Evaluation of a Learning Tool for In-Situ Monitoring of Metal Additive Manufacturing

Brent Valle[a,*], Karel Lietaert[b], Natania Antler[a], John Newman[a], Erik Xiao[a], Sam Coeck[b]

[a] KLA-Tencor Corporation, 1 Technology Drive, Milpitas, CA 95035, United States
[b] 3D Systems, Grauwmeer 14, 3001 Leuven, Belgium

Abstract:
This paper describes a multi-channel in-situ monitoring system developed to better understand defect formation signatures in metal additive manufacturing. Three high-speed imaging modes coupled with an image computer capable of processing and storing these data streams allowed an examination of defect formations signatures and mechanisms. It was found that defects later detected in x-ray computed tomography (CT) scans were related to regions with anomalous heat signatures and powder bed morphology. Automated defect detection algorithms based on these defect signatures captured 80% of defects greater than 300µm.

INTRODUCTION

Laser Powder Bed Fusion (LPBF) is an Additive Manufacturing (AM) process that can be used to realize geometries that would be difficult or impossible to manufacture using traditional methods. Within the last several years, LPBF has begun to transition from its rapid prototyping origins into production readiness. Several key barriers to increased adoption are lack of tools and education to (re)design for AM, high production cost, the need for extensive post-processing and the difficulty to qualify and maintain part quality [1].

The qualification and certification of AM components for the aerospace and naval industry with currently available tools can be very time-consuming and expensive [2, 3, 4, 5]. The current approach used in AM aims to freeze all possible process variables to establish a stable process [6]. As the number of variables in AM is very high, some could be missed and the manufacturing process could still shift over time. In the current approach, witness coupons are often tested to measure part quality. However, these coupons cannot be considered fully representative of the final part due to a difference in geometry and location in the production chamber [6]. In addition, the non-destructive tests (NDT) used in the non-AM industry might need to be changed before they can fully capture AM part quality. Problems in NDT of AM parts are mainly due to (i) the often complex part geometry, (ii) the lack of a defined critical defect type and size, (iii) the lack of physical NDT reference standards, (iv) the lack of written inspection procedures tailored to the AM process and (v) the lack of probability-of-detection data [7]. The availability of a proper process monitoring tool would help qualification by complementing NDT data and reducing the amount of NDT by rejecting faulty parts much earlier in the production chain [6].

Most of the available LPBF research has focused on optimization of laser power, scan speed, hatch spacing, hatch pattern etc. to produce dense parts and is thus aimed at avoiding defects. Less attention has been paid to defects themselves and the way they are formed [8, 9, 10]. Our approach is to provide an eye on the process that elucidates defect precursors or signatures. We envision this will guide process development and provide indicators to monitor the process.

To-date, in-situ process monitoring and defect detection efforts have explored a wide variety of sensors and imaging modalities. Among these are thermal imaging using coaxial [11, 12] and off-axis [13]

* Corresponding author at: KLA-Tencor, 1 Technology Dr., Milpitas, CA 95035, USA.
E-mail address: brent.valle@kla-tencor.com (B. Valle).

modes as well as visual imaging using coaxial [14] and off-axis [15, 16] modes. Pyrometry [17, 18], optical emission spectroscopy [19], fringe pattern projection [20] and optical coherence tomography [21] have also been employed. One of the challenges, especially for the high frame-rate imaging modalities, is the large quantity of data. This has led to efforts to reduce image data to simple parameters [11] [22], which can then be saved, visualized, and/or processed rather than the raw images. However, without a firm basis of understanding the signatures of defect formation, these data reduction strategies are premature. A lack of correlations between raw signals and defects has hindered the development of a deeper understanding of defect formation processes. Off-axis visual imaging of the powder bed has yielded the greatest success in its ability to detect gross warping and coating errors and is currently under adoption by several additive manufacturing OEMs. However, the tradeoff between resolution and powder bed coverage area limits detection of smaller defects.

To address the above gaps, an in-situ monitoring system was developed to maximize learning about defect formation and detection capability. The system was designed with the goal to gather information required to inform the requirements for future in-situ detection systems. Our approach was to develop a learning tool that can first begin to understand defect formation mechanisms and their signal signatures. Once the relevant signals have been identified and defect formation mechanisms are better understood, the sensitivity of signal channels to indications of defectivity can be quantified. Lastly this learning can be studied to extract the technical requirements for future in-situ detection systems.

The Experimental section of this paper provides an overview of the system architecture and integration, sensor channels, and data acquisition for the learning tool. The Results section illustrates several key advances in our progression towards understanding and detecting porosity defects. These illustrations include (i) observations of particle entrainment near the meltpool, (ii) detecting and localization of a landed spatter particle, (iii) examples of the most common defect formation signature, (iv) visualization tools that aid user detection of anomalous print locations, and (v) results of a study attempting to automate defect detection using image processing algorithms.

Two challenges that arose during this work are likely to be common in future studies of metal AM defects. The first, is the challenge of relying on computed tomography (CT) as a ground truth (generally accepted method to use as a benchmark) for porosity defects – especially for small pores. The second, is that the nature of the LPBF process can be self-healing, and separating porosity defects that persist from those that heal is likely to remain a significant challenge. In the final portion of the paper we discuss these and other hurdles.

EXPERIMENTAL DETAILS

Learning tool architecture overview

The first objective in developing the in-situ inspection learning tool is to acquire high lateral resolution, high frame rate images. Without firm foreknowledge of the relevant signals leading to defects, the requirements for the in-situ monitoring imaging system were derived from knowledge about the process. Beam velocity on the order of 1000 mm/s and relevant melt pool lateral dimension on the order of 10 s of microns requires frame rates in the 1000 s of Frames Per Second (kFPS) with 10s of micron lateral resolution. Fast melt pool dynamics [23, 24] also indicate the necessity for fast sampling. To achieve the required resolution in proximity of the melt pool as it traverses the powder bed, all signals are acquired coaxially with the process laser beam. Frame rates were achieved by reading out only sub-regions of the imaging sensor. To collect sufficient signal on the detector and to reduce back-reflections for the illuminated channel, the original galvanometer mirrors, protective window, and f-theta lens of a 3D

Systems ProX DMP 320 were replaced with broadband optical coated versions. The additional signal on the detector allowed the use of shorter integration times, which reduced motion blur, and narrower spectral filters, which reduced lateral and axial color shifts from the f-theta lens. More details about each of the imaging channels follows.

To maximize frame rates of the disparate sensors while maintaining data cohesion among channels and from the galvanometer position feedback data, a Field-Programmable Gate Array (FPGA) with 200 kHz base clock was used to send trigger signals to each frame-grabber and to acquire non-image printer metadata from a hardware interface to the printer designed specifically for this project. A user-customizable decimation factor for each camera determines the trigger rate for each channel. The highest frame rate used is for the Near InfraRed (NIR) channel at 50 kFPS. Galvanometer data is intercepted between the control board in the printer and the scan head. One coordinate of galvanometer data is received every 20 µs and is interpolated to have both x and y data at 50000 samples per second (S/s). An acquisition server reads FPGA data from a First In, First Out (FIFO) buffer and image data from frame-grabber queues by direct memory access.

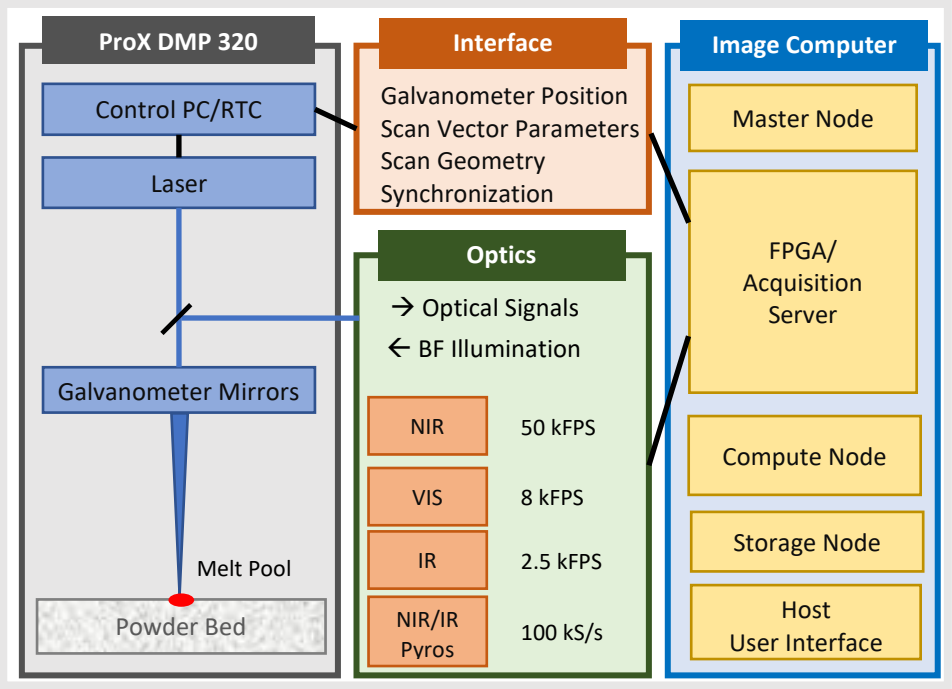

Fig. 1 Depicted is a simplified block diagram of the major subsystems of the in-situ monitoring system and its interface to the ProX DMP 320 printer. A modified image computer collects signals from the printer and the sensors on the optics plate. Optical and electronics interfaces to the printer allow the collection and acquisition of in-situ signals and printer control data. BF = BrightField, RTC = Real Time Computer, NIR = Near-InfraRed, VIS = Visible, IR = InfraRed, FPS = Frames Per Second , S/s = Samples per second, FPGA = Field-Programmable Gate Array.

After acquisition, the data is processed, and both the raw data and algorithm results are saved to disk using a modified image computer from a semiconductor bare wafer inspection system (KLA-Tencor Surfscan® series) designed for high-volume manufacturing. The image computer architecture is designed to efficiently collect, distribute and process images and related data. Compute power is sufficient to process dozens of frame algorithms on each acquired frame in real time. Data storage capacity is 1.3 PB, which at a data acquisition rate of 66 Gbit/s, provides 43.8 hours of raw data save time.

The saving of all raw data is a crucial feature of the learning tool as it allows prototyping of defect detection algorithms and scalar reduction of frame data. The ability to reprocess the same dataset with different algorithms or algorithm parameters and compare to known ground truth result such as CT proved to be a rapid way to design and tune algorithms. Our experimental approach is to examine defects formed in nominal or very near nominal process conditions. With these conditions defects are quite infrequent (on the order of 5-10 CT detected defects per cm^3) requiring samples on the order of several cm^3 to be printed to capture a significant number of defects.

Another key aspect of the in-situ inspection system design was to tightly integrate with the ProX DMP 320 (3D Systems), both in hardware and software. Hardware and software handshakes at the beginning of a print job ensured that the inspection system could be armed prior to the start of printing, that the data would be synchronized and that job data could be exchanged (this includes job metadata, scan vector geometry, and scan parameters). A hardware counter indicating the current vector number in the job in addition to this job information allowed data to be classified by part, scan parameter, scan vector types, direction, layer or other vector metadata. Other signals from the galvanometer control board included position information, commanded laser power control, and commanded laser on/off signals.

Learning tool optical channels

There are two types of signals acquired from the in-situ monitoring tool. The first is blackbody radiation from the melt pool where the emission spectrum is governed by Planck's law and the intensity at any point within the melt pool is determined by the temperature, temperature-dependent emissivity, and the local surface morphology of the melt pool. These signals are acquired using off-the-shelf NIR and InfraRed (IR) cameras and pyrometers. The second signal type is a quasi-brightfield channel illuminated by directly imaging the fiber tip of a high-brightness, fiber-coupled laser diode onto the powder bed. This signal is acquired using the brightfield (BF) camera.

Both signal types are collected using a coaxial optical configuration, where the imaging optical axes are shared with the process laser beam. The advantages of the coaxial configuration are that the imaging fields are simultaneously scanned with the process beam and that the cos(θ)-dependent off-axis intensity drop-off is symmetric about the center of the f-theta working field. The coaxial optical configuration also has several important challenges. One is the thermal light budget, which is hindered by a small numerical aperture (NA = 0.03), and black-body radiation spectral peak at longer wavelengths than most available fast Si-based camera sensors can capture. A related challenge is the fast beam velocity used in the LPBF process, which requires a short integration time to minimize motion blur.

A summary of the key parameters for each of the image channels is shown in Table I and an effective optical layout is depicted in Fig. 2.

Table I. Summary of key parameters for each optical channel.

Channel	Mode	Wavelength	Frame Rate	Object Pixel Size	ROI
		nm	kFPS	μm	pixels
NIR	Thermal	884 - 916	50.0	10	128 x 100
IR	Thermal	1175-1225	2.8	10	192 x 192
BF	Illuminated	660	8.3	5	384 x 384

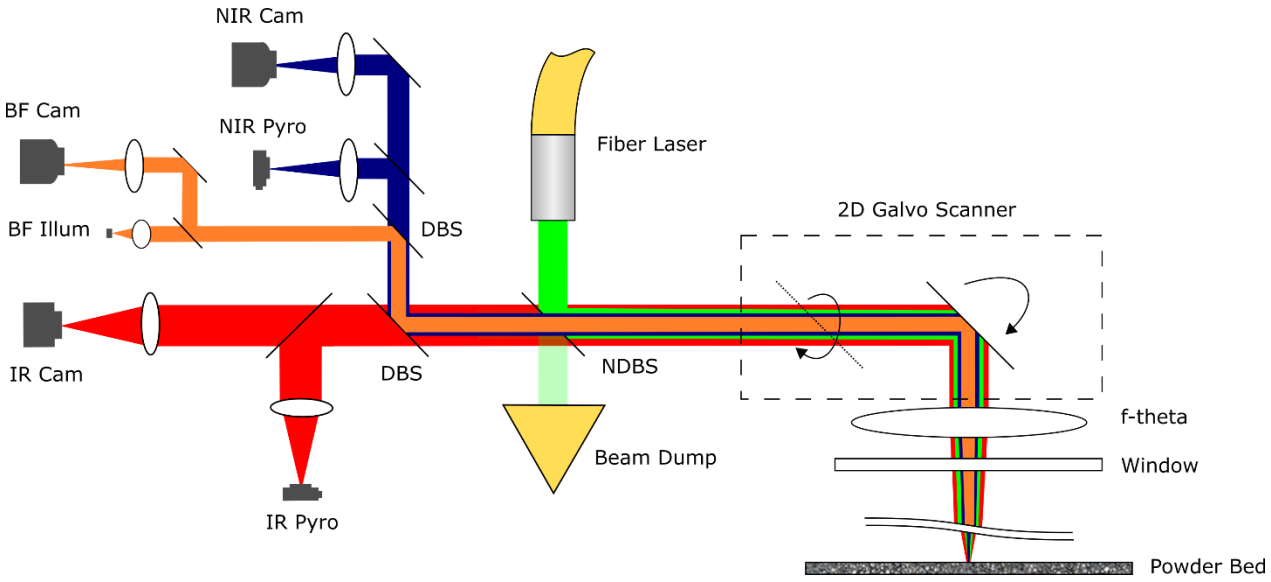

Fig. 2 The effective optical layout is shown. A narrow band notch dichroic beam splitter (NDBS) directs the 1070 nm process to the powder bed and allows in-situ signals to pass. Two dichroic beam splitters (DBS) are used to isolate the NIR, IR, and BF branches of the optical layout. Pickoff beam splitters direct portions of the IR and NIR signal to pyrometer photodiodes rather than the imaging camera sensors.

The decision on filter bandwidth and center wavelength selection was guided by three primary considerations. First, the optical throughput was maximized by increasing filter bandwidth and choosing a center wavelength that maximizes the product of camera Quantum Efficiency (QE), blackbody emission spectra, and transmission through the optical components between the detector and powder bed. Second, the lateral spot shift over the field of print caused by lateral color (second chromatic aberration, [25]) was minimized by choosing a center wavelength as close as practical to the f-theta design wavelength of 1070 nm. Third, spot blur at large deflection angles caused by lateral color was minimized by decreasing filter bandwidth.

The cameras used were flat field corrected using an integrating sphere before installation on the monitoring apparatus. Performance over the print field was characterized by measuring the size, shape, and lateral displacement within the camera fields of view of a round meltpool produced by using a beam velocity of 100 mm/s. Due to geometry, the image of the meltpool becomes elliptical as the scanner moves off axis. Similarly, the displacement of the meltpool centroid and meltpool image size in the radial direction were measured over the print field. As discussed above, the displacement and blurring of the meltpool image is caused by lateral color. To some extent these effects can be corrected through calibrations, but in these experiments, we found it more practical to restrict the field of print to a radius of 50 mm where the variation of the ellipticity, change in radial size, and centroid displacement of the melt pool image each varied by less than 10%. The approach of searching for local, relative changes to signals as defect candidate events mitigates the longer-range residual aberration present in our reduced field of print.

The NIR thermal channel captures the hottest portion of the melt pool and hot spatter ejected from the melt pool. The fast frame rate captures the melt pool dynamics and allows the tracking and characterization of spatter ejecta. The center wavelength of 900 nm was chosen to maximize the signal on the detector, which falls in the tail of the Si CMOS camera's falling quantum efficiency and rising melt pool thermal emission.

The IR thermal channel is used for imaging the cooler portions of the melt pool and solidifying melt pool tail. Because of the slower dynamics of the solidifying metal, a reduced frame rate can be tolerated so that the frame size can be increased. This allows a greater portion of the melt pool tail to remain in frame. The IR thermal channel also images the thermal emission of previously printed tracks. This can be used, for example, to locate points with anomalous cooling rates or hot spots from previous layers. Due to the insensitivity of Si at the wavelengths used, a fast InGaAs camera was used for acquiring data for this channel.

The BF illuminated channel behaves like a brightfield microscope imaging mode with some important differences. Due to the low numerical aperture of the imaging optics, the range of slopes that can be captured is quite limited. For this reason, portions of the image field at near normal incidence to the write beam will appear bright, other portions will appear dark. The non-telecentric f-theta lens will cause this slope to change as a function of scan position. Because the scene is composed of many spherical shaped powder particles and a very rough printed surface, this limited range of slopes that can be imaged still produces a feature rich image. Also because of the very rough surface, multiple reflections will cause some regions outside the slope limits to be visible, although only dimly. Lastly, even with filters rejecting light outside a narrow illumination band, blackbody radiation at the center of the melt pool is visible. Although undesirable, it is convenient for image registration between brightfield and thermal images.

Experimental approach

A well-calibrated (i.e. laser power, scanner, focal spot meeting manufacturer specifications) LPBF machine using nominal scan parameters to print Ti-6Al-4V alloy produces parts with relative densities >99.5 % [26]. Most of the remaining pores have a diameter smaller than 50µm and some are not detectable by micro-CT, even for relatively small and simple part geometries [27]. To address this infrequency of defects, others often deviate from nominal process condition to localize defective regions or to make correlations with degree of defectivity [28, 29]. We differ from this approach, because these non-nominal process conditions may produce defect signal signatures that are not representative of the nominal process. In fact, it may be that the defect formation mechanisms may be entirely different. For that reason, non-nominal process conditions were used only initially as a means of gaining knowledge about the signals observed. All later experiments to correlate signals with defects were conducted using nominal scan parameters on a well-calibrated LPBF machine. The approach is similar to a related study correlating melt pool events to mechanical properties of LPBF-produced tensile coupons [30].

To that end, the experiments below were performed on a 3D Systems ProX DMP 320 with the addition of the in-situ monitoring system. As discussed above, some of the optics were replaced, and subsequently the machine was recalibrated (laser power, scanner, focal spot) to factory performance. Tensile test coupons built after installation of the in-situ monitoring system performed according to ASTM F3001 [31]. The material used was Ti-6Al-4V grade 23 (LaserForm Ti Gr23, 3D Systems). Except for the data and discussion around the recoil ejection event (see Fig. 5), the layer thickness used was 60 µm, and 3D Systems' nominal scan parameters for the material were used. The sample geometry used for the defect sensitivity experiment was a pillar 25.0 mm in diameter and 28.8 mm in height. A notch running vertically and periodic ribs along the height of the cylinder were used as fiducial markings to register CT data to the galvanometer coordinate system. A depiction of the part is shown in Fig. 3.

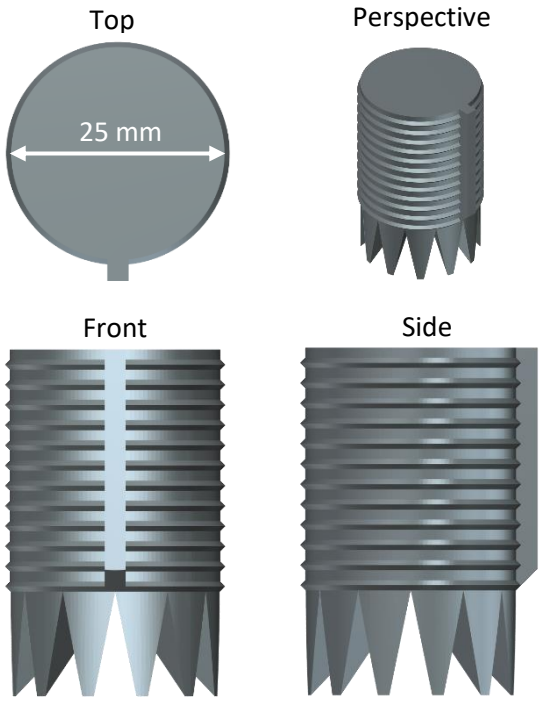

Fig. 3 A printed test volume consists of a cylinder 25 mm in diameter and 28.8 mm in height. 12 periodic ribs around the outside of the cylinder provide reference for position and scale in the vertical direction. Orientation of the cylinder in the CT volume is obtained using the notch running down the vertical face of the part. Solid supports ease the removal of the part from the baseplate and simulate the support and heat conductivity conditions representative of production parts.

CT scans of the as-printed samples were performed with a phoenix nanotom® m (General Electric Company) with a voxel size of 27 µm. Samples were then cut in four along the x and y directions and rescanned with a 21 µm voxel size to generate a higher resolution CT dataset. Data analysis was performed with VGSTUDIO MAX (Volume Graphics).

RESULTS AND DISCUSSION

Although highly dynamic and variable, the images from each channel have some consistent nominal features. As viewed in the thermal images the melt pool is teardrop shaped, with undulations and variability mostly in the tail region. The thermal images also capture hot spatter that are ejected from the melt pool. The brightfield scene with no printed material is mostly low gray levels, but speckled with small dots at the top of each powder grain. During printing, the unprinted material looks the same as above, but the printed material is also visible. The printed material is much more reflective, but because of its rough surface manifests as an area with widely varying dynamic range, from saturated to very low gray levels. Given the large dynamic range and the importance of simultaneously viewing both the printed and unprinted material, it can be convenient to view the logarithm of the brightfield image. Representative images depicting typical in-situ images under nominal print conditions for each channel are shown in Fig. 4 (movies available on https://3dsystems.sharefile.com/d-se0cd0f736c047ce8).

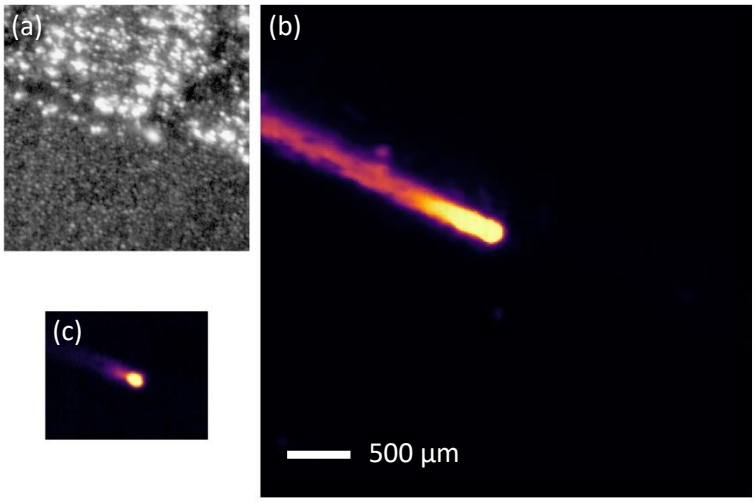

Fig. 4 In-situ frame data collected during nominal printing conditions and free from anomalies that will be discussed below. (a) the brightfield channel (contrast enhanced by taking the logarithm of the image) depicts printed and unprinted regions of the powder bed. (b) The IR thermal channel captures the cooling behind the melt pool tail. (c) The NIR channel images the molten, highly dynamic portion of the melt pool at a fast frame rate.

To characterize the signals observed under various print conditions, single tracks were printed on baseplates using a wide range in scan parameters. Beyond observing changes in melt pool size, shape, and spatter rates, another interesting melt pool behavior was detected. The melt pool images in Fig. 5 are extracted from the highest dose track (350 W laser power and 1000 mm/s scan speed), which offers the best view of the phenomenon due to the large melt pool acting as a thermal backlight. In the NIR frames, the scan direction is from the top of the frame to the bottom.

The first several images depict a dark agglomeration of powder particles (horizontal, red arrows). That the particles appear dark in these images indicate that they are cooler than the melt pool tail and are above the melt pool. The particles are resolved indicating their height above the melt pool is on the order of millimeters. The agglomeration is seen to be rotating end over end as they enter the bright portion of the melt pool. Then midway through the sequence, the agglomeration is heated and exits the melt pool region with a new velocity. Relative to 100 mm/s scan speed, the initial velocity and final velocity are 150 mm/s and 350 mm/s respectively.

These observations of ejecta redirection are consistent with the mechanism described previously as localized vapor recoil pressure on one side of the particle as it enters the laser beam [32]. The origin of the agglomeration is not readily apparent from the in-situ data. It is possible that the agglomeration was formed and launched into the air during a previously printed melt track. It could also be that the agglomeration was present in the powder and was entrained into the melt pool region by melt pool gas jets [33]. Incidentally, a similar event is observed as a powder particle enters from the front of the melt pool and is ejected in nearly the same direction (green, vertical arrows).

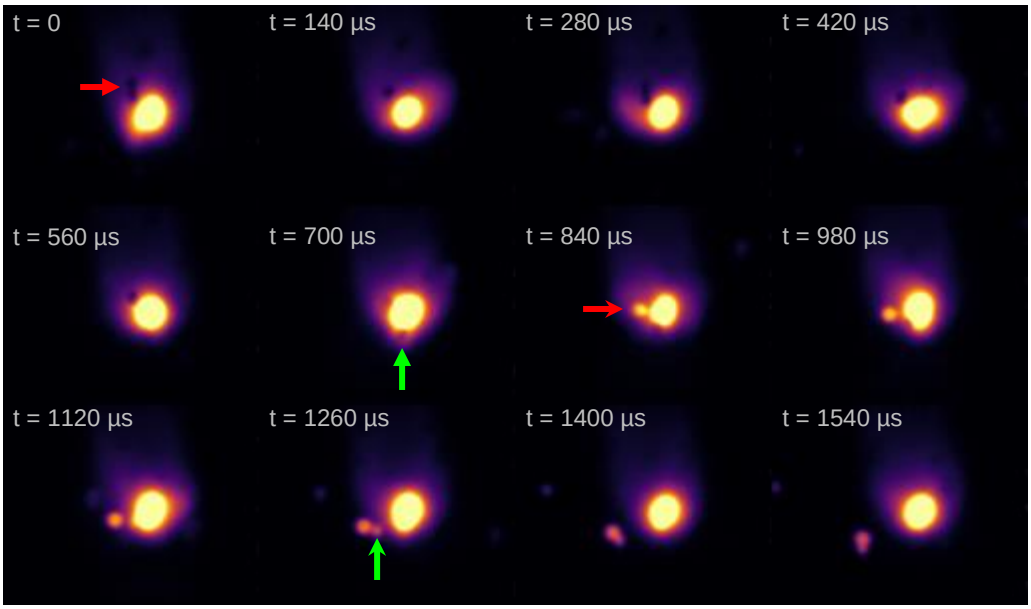

Fig. 5 A series of NIR camera images shows a cold particle entering the melt pool from the rear (red arrow), being heated and then redirected away from the melt pool by what we hypothesize as the vapor recoil pressure mechanism described in the full text. A similar event but with the cold particle entering from the front of the melt pool is also observed (green arrow).

Regardless of the origin of ejecta events, their presence can lead to defects in metal additive manufacturing production that detrimentally impact mechanical properties [34]. Therefore, understanding their formation, frequency and effects on printed structures is of interest to the AM community [33, 23, 34] and could lead to improved quality assurance systems and perhaps eventually to methods to improve print quality. One of the challenges to studying these questions about spatter particles is the difficulty to connect in-situ monitoring data of individual spatter events to the resulting spatter particle after it lands in the build area.

This paper's in-situ inspection system facilitates observation of the spatter event using in-situ data. For research purposes, further studies of the spatter particle can be conducted by interrupting the print and using the localization capabilities of the system. This is accomplished by observing ejecta events via thermal channels, and localizing the spatter particle using a combination of galvanometer position data, and brightfield images. After printing the layer to be studied, the part is removed and the brightfield images are registered to optical microscopy and SEM images. Below, in Fig. 6 (left), an ejecta particle is observed in the IR (green) and brightfield (gray) imaging channels over the course of four coincident frames. The particle is observed to land very near the stitch region of two printed areas. Post-print microscopy in this region allowed for the ejecta particle to be located and imaged. Scanning Electron Microscopy (SEM) micrographs are shown in the images on the right of Fig. 6 and indicate the size and morphology of the spatter particle.

The spatter particle is approximately 160 µm in diameter, which is considerably larger than the median powder particle diameter and is likely formed during the print. It is not known if the particle was formed during ejection from the meltpool or if the particle was formed earlier and was sitting in the powder bed. A loosely connected satellite particle and some surface contamination is observed on the surface of the large spatter.

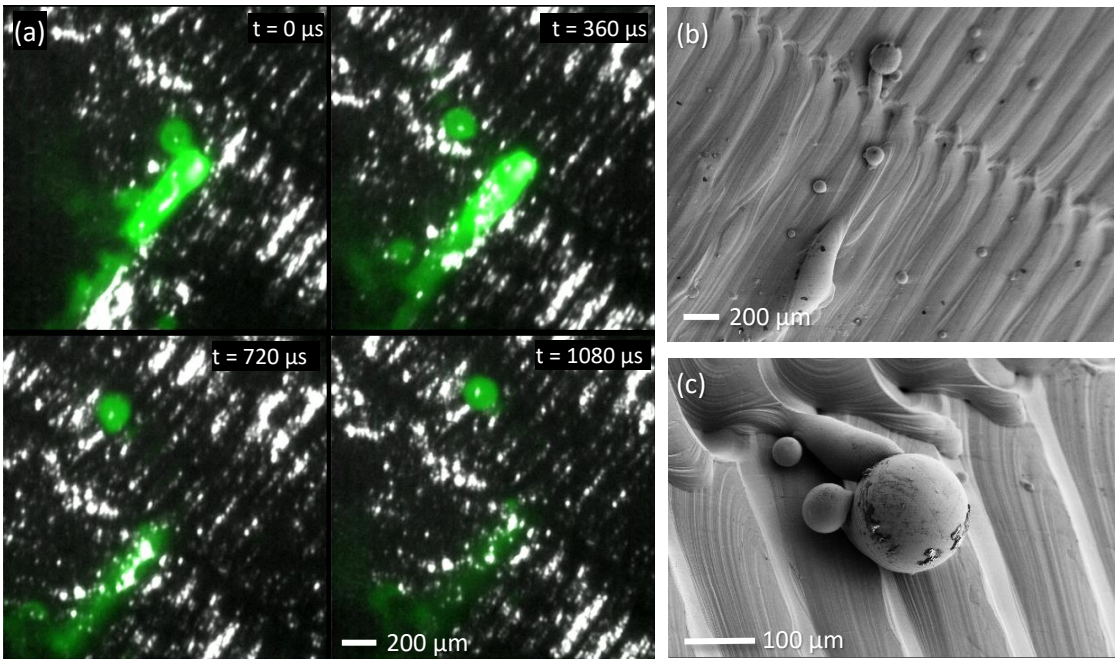

Fig. 6 In-situ and post-print observation of a large spatter particle. (a) These four images depict the fusion of brightfield (grayscale) and IR thermal channel (green). The images at 720 and 1080 µs depict the spatter particle's final location after it had landed on previously printed material. (b, c) Post-print SEM images in the vicinity of the landed spatter particle reveal the morphology of the spatter particle and surrounding printed material. The spatter particle is observed to be nearly spherical in shape, to have an attached satellite particle, and to have some surface contamination. SEM images were acquired using 5.0 kV accelerating voltage using the SE2 (type II secondary electron) channel.

The learning tool described above facilitated observations that are related to possible defect formation precursors; it also enabled traceback of voids discovered and localized by CT in the final part. Manual review of the data in the neighboring region of a defect as compared to normally printed regions was used to create heuristics for identifying signal signatures that are typically associated with defects. In short, two defect signatures that proved to be associated with defects will be described in the subsequent paragraphs.

In the IR channel, regions associated with CT voids often exhibited abnormally slow cooling rates. These regions can be observed as localized hot spots that often persist over the span of time that it takes to print multiple vectors and often multiple layers. The hot spot is often exacerbated when the melt pool collides with it, causing the melt pool to grow in area and often creating a shower of spatter particles. The top row of images in Fig. 7 depict roughly the same field of view corresponding to a CT defect event for several nearby write vectors. A faint hot spot is observed before any obvious interaction with the melt pool, and the hot spot becomes quite bright for several vectors that directly intersect with the event, and then only a faintly growing spot remains once the melt pool is no longer strongly interacting with the defect location.

In the brightfield channel, regions associated with CT voids often correspond with highly reflective spots in the unprinted powder region. After printing these regions become locally dark, often with a bright spot in the center. These two brightfield signatures are consistent with a large spatter or other contamination particle.

That these two defect signatures often coincide indicates that under the experimental conditions used (i.e., printing Ti-6Al-4V on a ProX DMP 320 using nominal process conditions) the voids that are observable

by CT are primarily formed by disturbances in the powder bed – likely from spatter formed within the current layer or from similar disturbances in previous layers. We have also observed that large defective regions can be created by a runaway process when the melt pool collides with these powder bed disturbances. The collision with the melt pool causes the ejection of more spatter particles onto the unprinted powder, and these new spatter particles then seed additional powder bed disturbances.

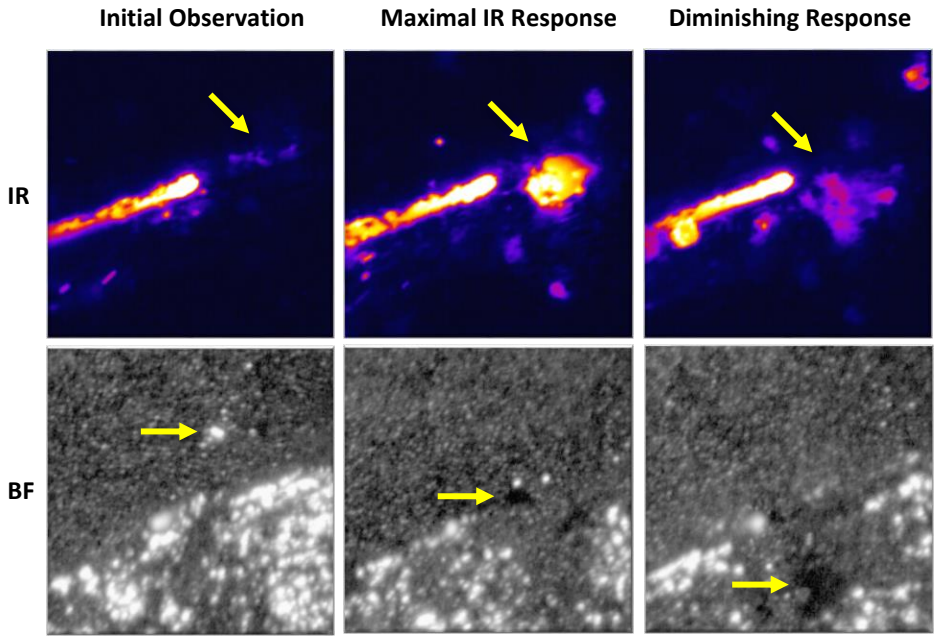

Fig. 7 Defect signature observations for a 770 µm diameter defect during the printing of layer 637 of the pillar test coupon. The IR signal response shows a residual hot spot in the powder bed. In the brightfield channel, an abnormal bright spot can be seen in the powder bed prior to printing. After printing that same location has an abnormal dark spot. Note that the BF channel is displayed in logarithmic scale.

Realizing that many of the events of interest were localized and stationary to the powder bed, and not the melt pool, visualization methods to aid users in identifying possible defective regions were developed. This proved to be fruitful as users could flag defects not detected by simple algorithms through visualization aids. The first of these visualization aids are scalar maps – where frame data is reduced to a small number of values that can be plotted spatially using galvanometer data. The second visualization aid is stitch maps – where frames or portions of frames are stitched to form a large aggregate image of the part. Because of the greater novelty of the approach as applied to metal AM, we will focus the following discussion on the method of producing and using stitch maps.

During the back-and-forth rastering of the beam during the infill portion of each printed part, the brightfield image can be segregated into a printed area and an unprinted area. These segmented images can then be placed into a part-sized image buffer using the galvanometer positions as a starting point with additional subpixel image registration refinement using cross-correlation techniques [35]. The two resultant images depict the unprinted powder bed and the final printed part. The unprinted image also contains contours and abutting regions between fill areas. Similar images can be captured using non-coaxial imaging of the powder bed, but with some important differences. The coaxial approach offers resolution nearly an order of magnitude greater than could be provided by a large megapixel camera mounted off-axis. In addition, because the unprinted area is imaged just before it is melted, spatter contaminants produced during printing of the current layer can be captured.

Similarly, the IR can be segmented and then stitched. As was seen in Fig. 7, the background region away from the meltpool can be indicative of defectivity. For that reason, the IR image is segmented into melt-pool and non-melt pool regions and then stitched into a part sized image. Stitching of the non-melt pool IR image helps to suppress spatter and briefly hot spots and helps to identify localized regions with abnormal heating.

Fig. 8 depicts the unprinted brightfield (a), non-melt pool IR (b) and printed bright-field (c) stitched images two layers above the defect shown in Fig. 7. For comparison, the CT slice from the same height is shown (d). The corresponding defect is in the lower-right portion of the part and is observed in all three images. In the unprinted brightfield channel, the bright semi-circular region corresponds to a multiple back-reflection of the illumination light in the f-theta lens. The defect aligns with the two bright spots surrounded by a dark region. The brightfield printed image also shows a dark spot where the defect is located. The non-melt pool IR image shows a large bright spot. The IR image also shows overheating of the short vectors (upper right and lower left of (b)).

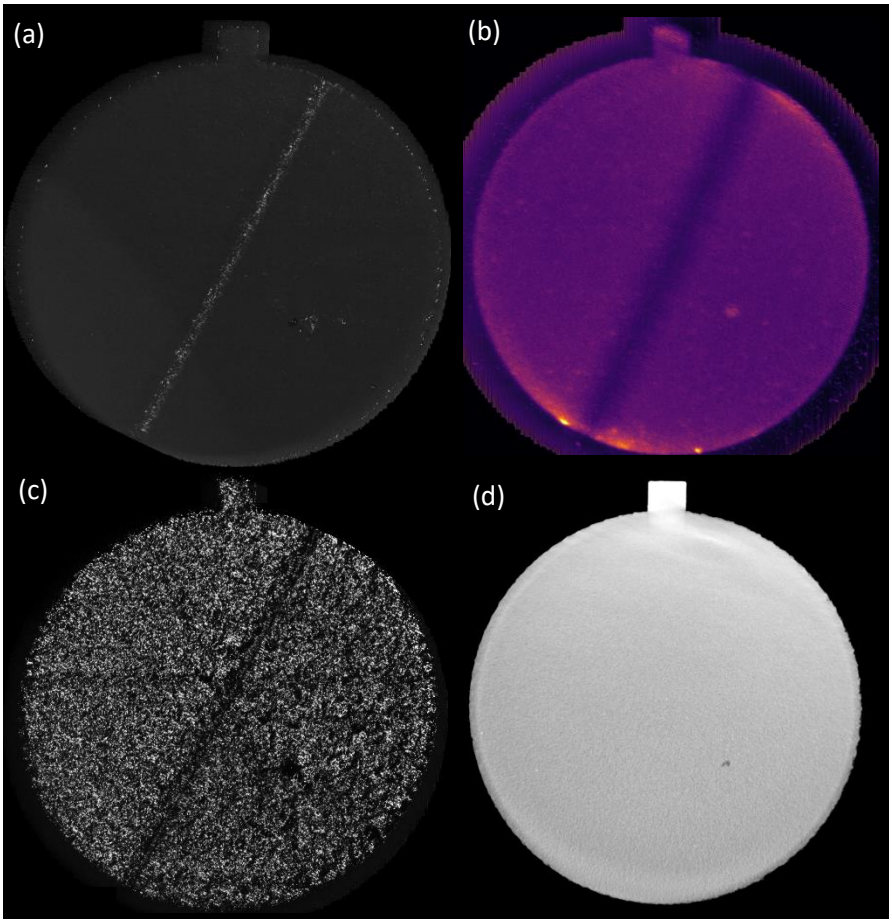

Fig. 8 Stitched maps for layer 639 of the pillar, which show the same defect as in Fig. 7 after two layers. (a) the unprinted BF map is built up during printing, which provides high-resolution imaging of the powder bed immediately before printing. (b) the IR background map is a thermal image, but with the melt pool removed. (c) the printed BF map is a high-resolution composite image of the part as printed. Although all are acquired during printing of the part's fill, it is helpful to regard these images in sequence: before (a), during (b), and after (c). (d) the corresponding CT slice.

These defect signature observations and stitch maps above informed the development of simple algorithms to flag likely defective regions. The IR algorithm records the location of anomalous events

consisting of a stationary hot spot above a size threshold that is observed in a user configurable number of frames and above a user configurable intensity threshold. The brightfield algorithm is similar in that it records the location of bright spots above an intensity threshold in the unprinted powder. These simple algorithms mimic the user observations that tend to capture larger defects (>500 µm). For users to detect smaller defects through manual review, they also utilized multiple layers (flipping back and forth between layers looking for persistent spots and shapes) or multiple channels. Although not utilized by the current set of algorithms, discussion about how these observations can be used to extend the current algorithms can be found later in this manuscript.

A study to understand the sensitivity of the system and algorithms to defects was conducted using micro-CT of the pillar parts described above. The CT defect report provides the location, size, and other shape parameters. Using the largest of either the x, y, or z dimension, the defects were binned by size. The coordinate systems of the CT and the in-situ monitoring system were registered using fiducial marks built into the design of the part. Of a print of 671 layers, from the CT defect report we identified 99 layers that contained pores. We chose 60 layers to subsample for our automated defect detection analysis. In-situ candidate events within 500 µm of a defect in the CT report were counted as captured defects. The overall defect capture rate was 80% for defects whose largest dimension was greater than 300 µm.

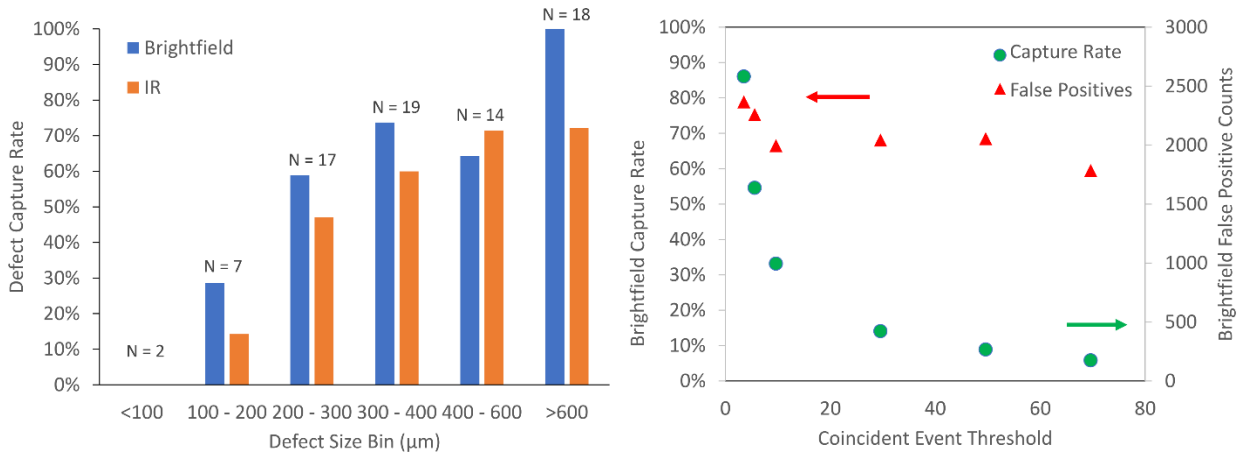

Fig. 9 (left) Defect capture rates versus binned defect size shows considerable drop off in defect sensitivity as defect size shrinks – falling below 50% capture rate around 300 µm. For each size bin the number of defects (N) is shown above the bar chart. (right) Overall capture rate and the number of false positive counts for the brightfield channel is plotted versus the Coincident Event Threshold, which is defined as the number of frames containing signal corresponding to the candidate event. The false positive count can be reduced significantly by filtering events with only a few frames of signal.

For defects smaller than 300 µm, the capture rate drops to 46% for the brightfield channel. A more detailed breakdown of capture rate versus defect size for this experiment is shown in Fig. 9. Manual review of the data suggests that for all but two defects, there is some observable signature, however the current algorithm designs and parameters are not able to capture them. In fact, we attempted to tune the algorithm thresholds to reduce false counts, but even after selecting an appropriate coincident event threshold (50 frames), the number of false counts remains about five times larger (266 false positives) than the total number of defects captured for the brightfield channel (53 captured defects). This substantial number of false counts can be explained by (i) an intrinsically noisy process that makes it difficult to separate process signal variability from defect signature signals, (ii) simple algorithm designs are not sufficient to differentiate defect signatures from natural process signal variability, (iii) events that we regard as “false counts” are actually real defects, but are not caught by CT, and (iv) defects are initially

formed and defect signatures are detected, but the printing of subsequent layers heal these defects so that they do not remain in the final printed sample.

On point (ii) above, that simple algorithms are not sufficient to the task, we have considered several paths for improvement. The first is to use multi-layer detection, not on the raw frame data, but on the stitch maps that have so far only been used for visualization and manual review. We expect that this multi-layer data can help to filter out false counts that do not persist over multiple layers. Another possible improvement direction is to utilize data fusion to utilize the multi-channel aspect of our dataset. The third approach is to develop a training dataset to develop machine learning algorithms to detect defects.

To explore point (iii) above, that some of our false counts might be defects, we sectioned the test coupon so that a higher resolution CT scan could be performed. Coupons were cut in 4 by sectioning along 2 cutting planes which were perpendicular to each other and contained the longitudinal central axis of the test coupon. The unsectioned CT defect report contained 77 pores. In the higher resolution CT, 315 new pores were obtained in the higher resolution CT, and 12 pores in the original CT were not detected in the rescan. A manual review of 10 randomly chosen events which were earlier regarded as false counts of the in-situ process monitoring system was conducted. Of these, all 10 were detected in the higher resolution CT rescan.

Future work should carefully consider the test coupon geometry when relying on CT as ground truth for porosity detection – especially when small defects are of interest. As discussed earlier, a large sample volume is required for a statistically significant number of defects to be present in material printed using nominal conditions. This is in opposition to CT resolution, which diminishes as sample size is increased. The use of several smaller test coupons, while more laborious, is one approach to solving this problem. Another fruitful area of future study would be to better quantify CT defect detection performance versus defect size, morphology, and type in metal AM samples using metallography as ground truth.

The confounding factor of self-healing, point (iv) above, is a challenging problem for metal AM in-situ monitoring. With information generally limited near the printing surface, distinguishing the signals of events that eventually heal from those that persist as defects in the final part will be difficult. One possibility is that the signals are available, and the challenge is then to build up a dataset and analysis revealing the features that can distinguish these two cases. The other possibility is that the signals between healed and non-healed defects are indistinguishable. In this case, the defect signature signal will only be able to flag possible problematic locations. It is still valuable to be able to flag defect precursors as the rate of these events can be used as a measure of print quality.

CONCLUSION

We have developed a multi-channel in-situ process monitoring system tightly integrated with a commercial LPBF system. Using that system, we have explored the capability to obtain information about defect formation precursors such as spatter particles through capturing in-situ process data and localization of the corresponding spatter. We have characterized common defect formation signatures corresponding to the nominal printing conditions in Ti-6Al-4V. This led to a study to examine the possibility of using simple algorithms to identify porosity defects in CT obtaining a capture rate of 80% for defects greater than 300 µm. We explored some of the difficulties in obtaining an accurate capture rate. One of the remaining unaddressed challenges is to better understand the healing of defects during the printing of subsequent layers.

Some of the key lessons learned during this study include: (i) The need to examine the printing process in the nominal or very near nominal condition. Defect formation mechanisms, defect types, defect sizes,

in-situ signal levels, and in-situ signal variability are all likely to be different in non-nominal process conditions, and that limits the usefulness of the data and conclusions obtained in those conditions. (ii) Developing proper test structures is important to conducting a successful experiment. We developed a large test volume to be sure to capture a statistically significant number of defects in nominal print conditions. This test volume required printed fiducial marks to register the CT volume to in-situ data. In hindsight, a similar test volume spread over several test coupons would have allowed for higher-resolution CT scans although at higher cost, complexity, and effort. (iii) Saving all the raw data enabled progress in the understanding of defect formation mechanisms. The ability to traceback and examine raw data around defects allowed the development of algorithms that were not conceived of prior to running the experiment.

Acknowledgements

This research did not receive any specific grant from funding agencies in the public, commercial, or not-for-profit sectors. The authors would like to thank the KLA-Tencor Corporate Technology Photo Physics Group for collecting the SEM images. The authors would like to thank Andy Hill, Kristof Joris, Damon Kvamme, Vincent Nguyen, Zhifeng Huang, Mike Berls, Edric Chen, Monica Ji, Xin Li, Mahendra Ramachandran, Roman Sappey, Paul Wieczorek, James Wu, Joshua Yang, Jan Tops, Jonas Van Vaerenbergh, and Frederik Verbist for their contributions in developing and integrating the learning tool with the ProX DMP 320.

REFERENCES

[1] M. Schröder, B. Falk and R. Schmitt, "Evaluation of Cost Structures of Additive Manufacturing Processes Using a New Business Model," in *Industrial Product-Service Systems Conference - PSS, industry transformation for sustainability and business*, Saint-Etienne, France, 2015.

[2] A. Peralta, M. Enright, M. Megadeh, J. Gong, M. Roybal and J. Craig, "Towards rapid qualification of powder-bed laser additively manufactured parts," *Integrating Mater. Manuf. Innovation,* vol. 5, no. 8, 2016.

[3] M. Seifi, A. Salem, J. Beuth, O. Harrysson and J. J. Lewandowski, "Overview of Materials Qualification Needs for Metal Additive Manufacturing," *JOM,* vol. 68, no. 3, 2016.

[4] U. D. o. T. F. A. Administration, "Summary Report: Joint Federal Aviation Administration–Air Force Workshop on Qualification/Certification of Additively Manufactured Parts," Jun 2016. [Online]. Available: http://www.tc.faa.gov/its/worldpac/techrpt/tc16-15.pdf. [Accessed 1 February 2018].

[5] D. GL, "Additive manufacturing - qualification and certification process for materials and components," November 2017. [Online]. Available: https://rules.dnvgl.com/docs/pdf/DNVGL/CG/2017-11/DNVGL-CG-0197.pdf. [Accessed 1 February 2018].

[6] N. Hrabe, N. Barbosa, S. Daniewicz and N. Shamsaei, "Findings from the NIST/ASTM Workshop on Mehanical Behavior of Additive Manufacturing Components," December 2016. [Online]. Available: https://doi.org/10.6028/NIST.AMS.100-4. [Accessed 31 January 2018].

[7] J. M. Waller, B. H. Parker, K. L. Hodges, E. R. Burke and J. L. Walker, "Nondestructive Evaluation of Additive Manufacturing - State-of-the-Discipline Report," November 2014. [Online]. Available: https://ntrs.nasa.gov/archive/nasa/casi.ntrs.nasa.gov/20140016447.pdf. [Accessed 31 January 2018].

[8] M. Grasso and B. M. Colosimo, "Process defects and in situ monitoring methods in metal powder bed fusion: a review," *Meas. Sci. Technol.,* vol. 28, 2017.

[9] E. Malekipour and H. El-Mounayri, "Common defects and contributing parameters in powder bed fusion AM process and their classification for online monitoring and control: a review," *Int. J. Adv. Manuf. Technol.,* pp. 1-24, 2017.

[10] S. K. Everton, M. Hirsch, P. Stravroulakis, R. K. Leach and A. T. Clare, "Review of in-situ process monitoring and in-situ metrology for metal additive manufacturing," *Mater. Des.,* vol. 95, pp. 431-445, 2016.

[11] T. Craeghs, F. Bechmann, S. Berumen and J.-P. Kruth, "Feedback control of Layerwise Laser Melting using optical sensors," *Physcs. Proc.,* vol. 5, pp. 505-514, 2010.

[12] S. Clijsters, T. Craeghs, S. Buls, K. Kempen and J.-P. Kruth, "In situ quality control of the selective laser melting process using a high-speed, real-time melt pool monitoring system," *Int. J. Adv. Manuf. Tech.,* vol. 75, p. 1089–1101, 2014.

[13] B. Lane, S. Moylan, E. P. Whitenton and L. Ma, "Thermographic measurements of the commercial laser powder bed fusion process at NIST," *Rapid Prototyping J.,* vol. 22, no. 5, pp. 778-787, 2016.

[14] P. Lott, H. Schleifenbaum, W. Meiners, K. Wissenbach, C. Hinke and J. Bültmann, "Design of an Optical system for the In Situ Process Monitoring of Selective Laser Melting (SLM)," *Physcs. Proc.,* vol. 12, pp. 683-690, 2011.

[15] S. Kleszczynski, J. zur Jacobsmühlen, J. T. Sehrt and G. Witt, "Error Detection in Laser Beam Melting Systems," in *23rd International Solid Freeform Fabrication Symposium*, Austin, Tx, 2012.

[16] T. Furumoto, M. R. Alkahari, T. Ueda, M. S. A. Aziz and A. Hosokawa, "Monitoring of Laser Consolidation Process of Metal Powder with High Speed Video Camera," *Physcs. Proc.,* vol. 39, pp. 760-766, 2012.

[17] M. Pavlov, M. Doubenskaia and I. Smurov, "Pyrometric analysis of thermal processes in SLM technology," *Physcs. Proc.,* vol. 5, pp. 523-531, 2010.

[18] H. Krauss, T. Zeugner and M. F. Zaeha, "Layerwise Monitoring of the Selective Laser Melting Process by Thermography," *Physcs. Proc.,* vol. 56, pp. 64-71, 2014.

[19] A. J. Dunbar and A. R. Nassar, "Assessment of optical emission analysis for in-process monitoring of powder bed fusion additive manufacturing," *Virtual Phys. Prototyp.,* vol. 13, no. 1, pp. 14-19, 2018.

[20] B. L. I. W. S. Z. J. D. A. Zhang, "In Situ Monitoring of Laser Powder Bed Fusion Additive Manufacturing Using Digital Fringe Projection Technique," in *American Society for Precision Engineering 30th Annual Meeting Proceedings*, Austin, Texas, 2015.

[21] G. Guan, M. Hirsch, Z. H. Lu, D. T. D. Childs, S. J. Matcher, R. Goodridge, K. M. Groom and A. T. Clare, "Evaluation of selective laser sintering processes by optical coherence tomography," *Mater. Des.,* vol. 88, pp. 837-846, 2015.

[22] T. Craeghs, S. Clijsters, J.-P. Kruth, F. Bechmann and M.-C. Ebert, "Detection of Process Failures in Layerwise Laser Melting with Optical Process Monitoring," *Physcs. Proc.,* vol. 39, pp. 753-759, 2012.

[23] S. K. Khairallah, A. T. Anderson, A. Rubenchik and W. E. King, "Laser powder-bed fusion additive manufacturing: Physics of complex melt flow and formation mechanisms of pores, spatter, and denudation zones," *Acta Mater.,* vol. 108, pp. 36-45, 2016.

[24] C. Zhao, K. Fezzaa, R. W. Cunningham, H. Wen, F. De Carlo, L. Chen, A. D. Rollett and T. Sun, "Real-time monitoring of laser powder bed fusion process using high-speed X-ray imaging and diffraction," *Sci. Rep.,* vol. 7, 2017.

[25] B. H. Walker, Optical Engineering Fundamentals, SPIE Press, 2009.

[26] L. Thijs, F. Verhaeghe, T. Craeghs, J. Van Humbeeck and J.-P. Kruth, "A study of the microstructural evolution during selective laser melting of Ti-6Al-4V," *Acta Mater.,* vol. 58, pp. 3303-3312, 2010.

[27] S. Leuders, M. Thöne, A. Riemer, T. Niendorf, T. Tröster, H. Richard and H. Maier, "On the mechanical behaviour of titanium alloy TiAl6V4 manufactured by selective laser melting: Fatigue resistance and crack growth performance," *Int. J. Fatigue,* vol. 48, pp. 300-307, 2013.

[28] S. Betts, "Evaluation of Quality Signatures using In-Situ Process Control during Additive Manufacturing with Aluminum Alloy AlSi10Mg," 27 November 2017. [Online]. Available: https://www.sigmalabsinc.com/sites/default/files/2017-11/Evaluation%20of%20Quality%20Signatures%E2%84%A2%20using%20In-Situ%20Process%20Control%20during%20Additive%20Manufacturing%20with%20Aluminum%20Alloy%20AlSi10Mg_Rev4.pdf. [Accessed 31 January 2018].

[29] T. Toeppel, P. Schumann, M.-C. Ebert, T. Bokkes, K. Funke, M. Werner, F. Zeulner, F. Bechmann and F. Herzog, "3D Analysis in Laser Beam Melting Based on Real-Time Process Monitoring," in *Materials Science and Technology*, Salt Lake City, Utah, USA, 2016.

[30] N. R. F. V. S. C. Manisha Bisht, "Correlation of selective laser melting-melt pool events with the tensile properties of Ti-6Al-4V ELI processed by laser powder bed fusion," *Addit. Manuf.,* vol. 22, pp. 302-306, 2018.

[31] ASTM International, ASTM F3001-14, Standard Specification for Additive Manufacturing Titanium-6 Aluminum-4 Vanadium ELI (Extra Low Interstitial) with Powder Bed Fusion, West Conshohocken, PA: ASTM International, 2014.

[32] M. J. Matthews, G. Guss, S. A. Khairallah, A. M. Rubenchik, P. J. Depond and W. E. King, "Denudation of metal powder layers in laser powder bed fusion processes," *Acta Mater.,* vol. 114, pp. 33-42, 2016.

[33] S. Ly, A. M. Rubenchik, S. A. Khairallah, G. Guss and M. J. Matthews, "Metal vapor micro-jet controls material redistribution in laser powder bed fusion additive manufacturing," *Sci. Rep.,* vol. 7, p. 4085, 2017.

[34] M. T. Andani, R. Dehghani, M. R. Karamooz-Ravari, R. Mirzaeifar and J. Ni, "Spatter formation in selective laser melting process using multi-laser technology," *Mater. Des.,* vol. 131, pp. 460-469, 2017.

[35] S. T. T. a. J. R. F. Manuel Guizar-Sicairos, "Efficient subpixel image registration algorithms," *Opt. Lett.,* vol. 33, pp. 156-158, 2008.

[36] R. J. Smith, M. Hirsch, R. Patel, W. Li, A. T. Clare and S. D.Sharples, "Spatially resolved acoustic spectroscopy for selective laser melting," *Journal of Materials Processing Technology,* vol. 236, pp. 93-102, 2016.